Optical Nanoimpacts of Dielectric and Metallic Nanoparticles on Gold Surface by Reflectance Microscopy: Adsorption or Bouncing?

Jean-François Lemineur, Talia Jane Stockmann, Jérôme Médard, Claire Smadja, Catherine Combellas, Frederic Kanoufi

Optical Nanoimpacts of Dielectric and Metallic Nanoparticles on Gold Surface by Reflectance Microscopy: Adsorption or Bouncing?

Jean-François Lemineur[1] · Talia Jane Stockmann[1,2] · Jérôme Médard[1] · Claire Smadja[3] · Catherine Combellas[1] · Frédéric Kanoufi[1]

Abstract

Optical modeling coupled to experiments show that a microscope operating in reflection mode allows imaging, through solutions or even a microfluidic cover, various kinds of nanoparticles, NPs, over a (reflecting) sensing surface, here a gold (Au) surface. Optical modeling suggests that this configuration enables the interferometric imaging of single NPs which can be characterized individually from local change in the surface reflectivity. The interferometric detection improves the optical limit of detection compared to classical configurations exploiting only the light scattered by the NPs. The method is then tested experimentally, to monitor in situ and in real time, the collision of single Brownian NPs, or optical nanoimpacts, with an Au-sensing surface. First, mimicking a microfluidic biosensor platform, the capture of 300 nm FeOx maghemite NPs from a convective flow by a surface-functionalized Au surface is dynamically monitored. Then, the adsorption or bouncing of individual dielectric (100 nm polystyrene) or metallic (40 and 60 nm silver) NPs is observed directly through the solution. The influence of the electrolyte on the ability of NPs to repetitively bounce or irreversibly adsorb onto the Au surface is evidenced. Exploiting such visualization mode of single-NP optical nanoimpacts is insightful for comprehending single-NP electrochemical studies relying on NP collision on an electrode (electrochemical nanoimpacts).

Keywords Reflection microscopy · Single nanoparticle · Sensor · Adsorption · Silver · Polystyrene

1 Introduction

Many sensors rely on a recognition event often due to the interaction of an analyte with a sensing surface; electrochemical sensors and electrodes are some of them. However, defects or domains of heterogeneous reactivity are often present on sensing surfaces impacting the overall sensor performances. As the sensors rely on a macroscopic measurement, such as a macroscopic current or potential response in the case of an electrode, it is crucial to be able to recognize spatially their heterogeneous activity, while the sensing reaction is operating. In this respect, different electrochemical strategies are proposed to map and quantify localized (electro)chemical activity of surfaces.

On one hand, the (electro)chemical activity of a surface can be mapped using scanning electrochemical probe microscopies (SEPMs) such as the scanning electrochemical microscopy which uses a micro/nanoelectrode to map the electrochemical activity of a surface [1]. More recently with the scanning electrochemical cell microscopy [2], a nanodroplet is spread over a surface forming a micro/nanosized electrochemical cell. These methods allow probing and mapping heterogeneities of surface, regarding their electrochemical reactivity, with sub-100 nm resolution.

On the other hand, optical microscopies have opened alternative ways to image (electro)chemical and sensing processes. These microscopies combined to electrochemical processes, or equivalently surface recognition processes, which are able to quantify and map chemical surface transformations with sub-diffraction limit resolution and sub-molecular layer sensitivities. One of their advantages

✉ Frédéric Kanoufi
frederic.kanoufi@univ-paris-diderot.fr

[1] Université Sorbonne Paris Cité, Université Paris Diderot, ITODYS, CNRS UMR 7086, 15 rue J.A. de Baïf, 75013 Paris, France

[2] Present Address: Memorial University of Newfoundland, Chemistry Department, 283 Prince Philip Dr., St. John's, NL A1B 3X7, Canada

[3] Faculty of Pharmacy, University Paris-Sud, CNRS UMR 8612, 5 rue J.B. Clément, 92296 Châtenay-Malabry, France

compared to SPEMs is their high-throughput imaging as a large surface area ($>50\times50$ μm^2) can be fully imaged and analyzed at the pace of a camera acquisition rate (up to kHz).

Apart from microscopies relying on spectroscopic identification, such as enhanced Raman spectroscopies (SERS or TERS), or on the use of a fluorescent tag, label-free techniques have been proposed. Among them, microscopies based on the change in surface plasmon resonance, SPR, are able to image the local change of refractive index associated, e.g., with a heterogeneous chemical transformation occurring at the upper sensing surface of a planar Au film. Such local chemistry or local refractive index change perturbs the surface plasmon wave propagating in the Au film when it is illuminated (from its lower side). This perturbation is detected as a local perturbation of the reflected beam and is collected by a camera. Popular in biochemical studies, SPR was also combined with electrochemistry, and more recently as a microscopy to image heterogeneous electrochemical currents at microstructured electrodes or the electrochemistry of single NPs [3–8].

The detection and study of single NPs in an electrochemical environment can also be reached by exploiting optical scattering properties. Under dark-field illumination, the change in the NP-localized SPR upon electrochemical activation has allowed imaging various electrochemical processes at the single-NP level in 2D [9–11] or 3D [12–14], even though this method is often limited to >40 nm plasmonic NPs.

Other optical strategies can be proposed to image heterogeneous electrochemical processes from local changes in refractive index. Quantifying the change in light reflectivity is an appealing one. Ellipsometry is largely employed in the characterization of optical properties in material science; for example, ellipsometric microscopy [15] allowed imaging local molecular electrochemical transformation of Au surfaces. Simpler and yet quantitative strategies consist in analyzing images collected by a standard microscope operating in the reflection mode. Indeed, our group showed that the analysis of the light reflected by a reflecting surface illuminated under normal incidence [16–18], allowed quantifying and mapping heterogeneous electrochemical processes with sub-monolayer formation or deposition sensitivity. Particularly, we demonstrated the versatility of the strategy to the in situ imaging, using water-immersion objectives, of various electrode systems such as microfabricated Au-coated Si wafer [17], the standard glass-shielded microelectrodes [16], or various electrode materials, such as iron [18], for operando corrosion studies. Herein, we propose to extend this simple and versatile reflectivity microscopy to the direct in situ imaging of individual NPs.

It is expected that such imaging relying on the change in light reflectivity of a sensing (reflecting) surface yields high sensitivity in terms of NP detection and imaging. Visualization of the NP light scattering in a reflection mode has several advantages compared to the most common visualization operated in transmission mode (as usually performed under classical dark-field illumination). As illustrated in Fig. 1a, when a NP is immobilized on a reflecting surface, here an Au-coated Si wafer, the light reflected by the surface may constructively interfere

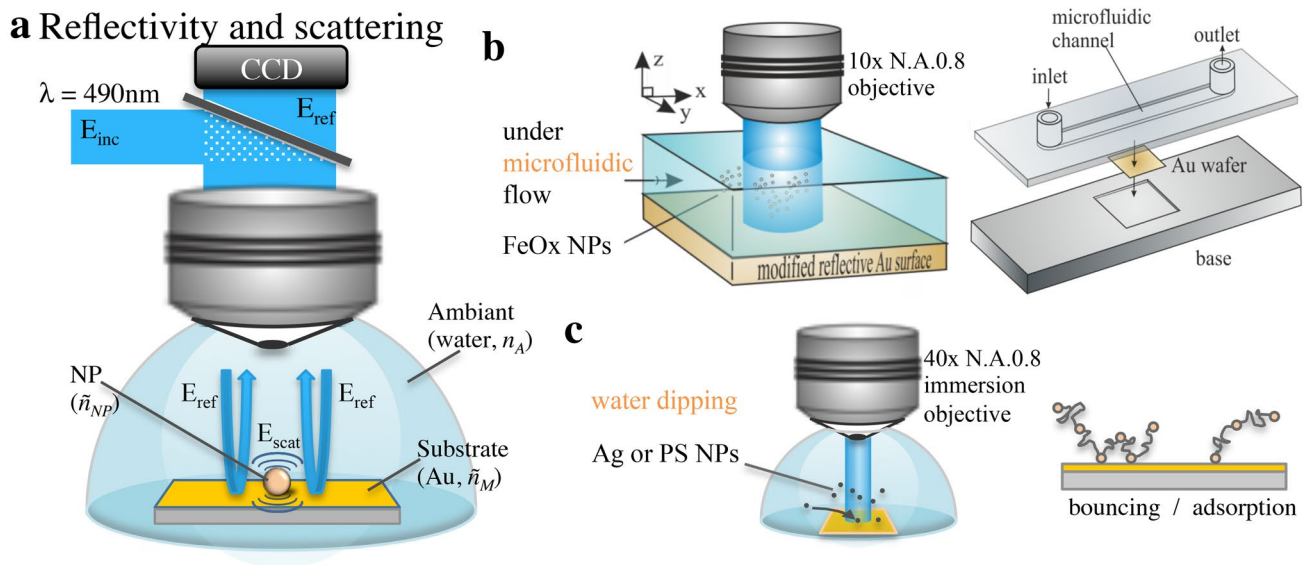

Fig. 1 **a** Principle of reflectivity imaging of scattering NPs at a gold-reflecting surface. **b**, **c** Schematic experimental configurations used for the monitoring (**b**) of 300 nm FeOx maghemite NPs convection-adsorption in a microfluidic cell or **c** of the bouncing or irreversible adsorption of 40 and 60 nm Ag, or 100 nm PS NPs on a surface

with the light back-scattered by the illuminated NP. Such reflection imaging microscopies exploit interferometric [19–30] detection principles. They yield enhanced NP visualization with sensitivities, which have outperformed dark-field observations in some configurations named iSCAT [21–23], SP-IRIS [24–26], BALM [28–30], for, respectively, interferometric SCATtering microscopy, Single Particle Interferometric Reflectance Imaging Sensor, or Backside Absorbing Layer Microscopy. These methods have unprecedented sensitivities allowing the detection of down to 10 nm individual NP. Among them, the BALM technique is the only one exploiting such detection over a conductive surface (an ultrathin Au layer), which can be of interest for single-NP electrochemical studies [28–30].

The present work shows that the simple reflectivity of a semi-infinite Au surface offers interesting performances for in situ single-NP visualization. For this purpose, we first establish an optical modeling of the operating principle. This extends the model proposed from the similar SP-IRIS technique [24–26], however, adapted to the water-Au interface. It is exemplified for various NPs: absorbing iron oxide maghemite, FeOx, NPs, dielectric ones from polystyrene, PS, then metallic ones, such as Ag NPs. The model predicts that reflectivity imaging is particularly sensitive to the visualization of dielectric NPs with predicted detection limit for PS or Ag NPs down to 30 nm, competing with current dark-field imaging techniques.

We then confirm experimentally this potentiality by monitoring the adsorption from colloidal solution of 300 nm FeOx NPs, 100 nm PS or 40 and 60 nm Ag NPs on a reflecting Au surface. This is performed under two experimental conditions presented in Fig. 1. The first example (Fig. 1b) shows how the technique can be employed to monitor the capture of individual magnetic FeOx nanobeads by a biosensor in a microfluidic environment [31]. The second example (PS and Ag NPs, Fig. 1c) is more relevant to the electrochemical nanoimpact strategies used to detect, characterize and count individual NPs [32–34]. A question often considered in this emerging electroanalytical field concerns the dynamics of the NP motion associated to its electrochemical actuation at a detecting electrode. Herein, we propose to address this issue in the absence of electrochemical transformation, by optically monitoring the interaction of Ag or PS NPs at a non-polarized Au surface. More specifically, we present the influence of electrolyte on the ability of NPs to repetitively bounce or irreversibly adsorb onto the Au surface. Although not performed in an electrochemical environment, the results will be of interest in comprehending and developing useful physical insight into single-NP electrochemical studies.

2 Experimental

The detection of individual NPs freely moving in solution or adsorbed on an Au-coated Si wafer (Aldrich) was investigated in real time by light reflectivity microscopy. It was performed, as previously described [16–18], with an in-house developed setup consisting of a standard microscope (Olympus) equipped with a water-immersion objective (Olympus LUMPLFLN 40XW, 40×, NA 0.8), and a CCD camera (PhotonFocus MV-D1024E-160-CL). A light halogen source, filtered at 490 nm with an interference filter (spectral bandwidth of 20 nm), was used to illuminate, from the top solution and via the objective, the Au substrate. The reflected light, collected from the same objective, was sent to the CCD camera. Before experiments, the illumination incidence on the substrate surface to be imaged was adjusted with an accuracy of 0.01°, in the absence of solution, using an interference Mirau objective (Nikon, CF Di 20×NA 0.4) by minimizing interference patterns. The colloidal solutions, prepared from commercial NPs solutions (FeOx from Ademtech®, PS NPs from Aldrich®, Ag NPs from NanoComposix®) were then poured into the homemade cell for in situ observation. The images of the reflecting surface on the CCD camera were captured through a home-programmed Labview software. Each image is a stack of five snapshots, each integrated over 50 ms. Each image is then taken every 1.86 s. Image analysis was achieved using Matlab routines.

3 Results and Discussion

3.1 Theoretical Background

3.1.1 Principle of the Reflectivity Measurement

Consider an electromagnetic planar wave, characterized by an incident electric field E_{inc}, propagating in an ambient medium A (of refractive index n_A) towards a reflecting substrate M (of complex refractive index $\tilde{n}_M = n_M + i\,k_M$). Upon reflection, the reflected planar wave is characterized by an electric field E_{ref} whose properties are given by Fresnel laws. Particularly, the signal $I(x,y)$ recorded at each pixel location, x, y, at a detector (a CCD camera) corresponds to the modulus of the reflected field, $|E_{ref}(x,y)|^2$. For normal incidence, the reflectance, R, which characterizes the amount of light reflected by the surface, is given from the Fresnel equation by,

$$R = \frac{|E_{ref}|^2}{|E_{inc}|^2} = \left|\frac{n_A - \tilde{n}_M}{n_A + \tilde{n}_M}\right|^2. \quad (1)$$

In its simplest form, the incident light flux is not evaluated, and only the reflected light is collected on a CCD. Relative reflectance measurements are obtained by comparing

successive images or times, t, as long as the incident illumination is kept constant. Comparing the signal recorded at each pixel $I(x,y,t)$ to that recorded on the first image $I(x,y,t=0)$ allows monitoring of the local relative variation in reflectivity, $\Delta R(x,y,t)/R$, from,

$$\frac{I(x,y,t)}{I(x,y,t=0)} = \frac{R(x,y,t)}{R(x,y,t=0)} = 1 + \frac{\Delta R(x,y,t)}{R(x,y,t=0)}. \quad (2)$$

Under the $\lambda = 490$ nm blue light illumination used herein, an ideal reflecting Au substrate ($\tilde{n}_{M.} = 1.1 + 1.83i$) immersed in water ($n_A = 1.33$) is expected to reflect toward the CCD camera 37% of the incident light, and our setup was shown to detect local variation of reflectivity down to $\Delta R/R = 0.002$ [16–18], meaning variation in collected signal down to 0.2%.

3.1.2 Nanoparticle Detection by Reflectance Imaging Microscopy

One prospect of the enhancement of small NP visualization (Fig. 1a) is due to the fact that the field scattered by the NP is a spherical wave while the incident (or reflected) field is a plane wave. The signal $I(x,y)$ recorded at each pixel corresponds to the interference pattern of the back-scattered far-field E_{scat} and a reference field, here the reflected field, E_{ref}, and $I(x,y)$ writes:

$$I(x,y) = \left|E_{ref}(x,y) + E_{scat}(x,y)\right|^2, \quad (3)$$

$$= \left|E_{ref}(x,y)\right|^2 + \left|E_{scat}(x,y)\right|^2 + \left|E_{ref}(x,y)\right|\left|E_{scat}(x,y)\right|\cos(\phi), \quad (4)$$

where ϕ is the phase lag between both fields. While for a NP of diameter d_{NP} the scattering signal $\left|E_{scat}(x,y)\right|^2$ usually scales as d_{NP}^6, for small NPs the preponderant signal arises from the interference term (last term in Eq. 4) and scales as the scattered field amplitude $\left|E_{scat}(x,y)\right|$ and, therefore, as d_{NP}^3. It thus enables the detection of much smaller nanoobjects than under dark-field illumination, enabling the real time and operando inspection of NP with sensitivity similar to standard scanning electron microscope [28].

The quantitative simulation of such interferometric far-field NP visualization has been proposed by Ünlü's group [24–26]. They modeled by boundary element methods, BEM, the SP-IRIS configuration where a NP is immobilized on a flat multilayer substrate, made of a thin SiO_2 dielectric layer onto a reflective Si semi-infinite substrate. The NP is imaged from the top, in a reflection mode in an air medium. This configuration applies straightforwardly to the present case, more pertinent for electroanalytical applications, where a NP immobilized onto a flat Au substrate is imaged, from a top solution, through a water-immersion objective.

The adapted optical model, precisely described in Ref. [24–26], briefly consists of simulating the steady-state optical scattering of NPs on a reflecting substrate, by solving Maxwell's equations via discrete numerical methods. BEM is preferred as it considerably speeds up the calculation process because it only requires the meshing of the different NP-medium interfaces (and not the whole volume as in finite element methods such as COMSOL®). Moreover, a Matlab toolbox dedicated to the simulation of the scattered fields of nanoparticles on layered media is available online through the Magnetic Nanoparticle Boundary Element Method (MNPBEM) implementation [35–39]. It is implemented for a wide range of examples and codes for the SP-IRIS situation that are also available online [38]. Modification of the latter codes to account for our experimental configuration is straightforward. Mostly, the ambient medium is changed from air to water ($n_A = 1.33$), the substrate is changed from layered SiO_2/Si to Au (with refractive index obtained from literature [40]).

Typically, the geometry of the system is first defined: a monochromatic ($\lambda = 490$ nm) incident plane wave E_{inc} illuminates at normal incidence a NP of various materials (Ag, PS, Fe_3O_4; refractive indexes, $\tilde{n}_{NP}$, are, respectively, $\tilde{n}_{Ag} = 0.135 + 2.71i$, $n_{PS} = 1.61$ and $\tilde{n}_{Fe_3O_4} = 2.36 + 0.07i$, based on literature data [40]) immobilized on a semi-infinite Au substrate. In a first approach, the illumination was considered as a single plane wave. A more rigorous approach would consider the decomposition of the illumination source into different incoherent plane wave components with different incident angles. The overall image would then correspond to the superposition of the response of each of these individual components [24].

In the simpler approach proposed here, the far-field image collected on the detector is obtained from the interference of the normal incidence reflected plane wave (E_{ref}) with the corresponding induced scattered field. The reflected field is obtained from the Fresnel formalism, as in Eq. (1). The MNPBEM toolbox is used to compute the far-field scattering E_{scat} propagating along the whole microscope objective's (NA = 0.8) collection solid angle. Finally, the image at the detector I(x,y) is obtained from Eq. (3) by coherently adding both reflected and scattered contributions at each pixel position (x, y) of the image plane.

3.1.3 Simulated Images of Nanoparticles by Reflectance Imaging Microscopy

As detailed in Ünlü's work, the images of NPs by reflectance microscopy depend on the properties of the NP material versus that of the reflecting substrate, but also on the NP to substrate distance and on the defocus of the observation. Figure 2 presents the simulated optical responses of NP materials chosen here. The simulated reflectivity images of a 40 nm metallic Ag NP and a 100 nm dielectric PS NP are given, respectively, in Fig. 2a, b, while the reflectivity

profile line of all materials (including the absorbing dielectric FeOx NP) for d_{NP} ranging from 30 to 100 nm are presented in Fig. 2c–e. Over the Au-reflecting substrate, both PS and FeOx NPs are detected as negative contrast features, while the metallic NP appears as a bright contrast one. Actually, the detection and the contrast of NPs depend on the refractive index of the NP material with respect to that of the substrate. For example, the presence of Au NP would be undetected on the Au substrate. Similarly, by changing the Au-reflecting substrate to the SiO_2-coated Si substrate employed in the SP-IRIS configuration, the NP contrasts become inverted: in SP-IRIS a metallic Ag NP (respectively, a dielectric PS NP) would appear as a negative (respectively, positive) feature.

In the case of the Au-reflecting substrate, illumination at $\lambda = 490$ nm allows the highest contrast, since it is the spectral region where Au is the least refractive (highest signal-to-noise ratio). Typically, the detection limit of $\Delta R/R > 0.002$ suggests that 25 nm Ag NPs can be imaged individually at $\lambda = 490$ nm, while 100 nm Ag NPs would not be detected ($\Delta R/R = 0.0007$) on an Au substrate illuminated at $\lambda = 633$ nm.

3.2 Experimental Illustrations of Reflectance Imaging Microscopy of Nanoparticles on Au Substrates

This section presents the ability of reflectance microscopy for analytical and electroanalytical case studies devoted to the imaging of the interaction of NPs with Au surfaces. Two experimental examples are presented, which display the monitoring of the individual NP behavior in colloidal solutions above an Au surface. Although no electrochemical actuation is performed here, the examples show the collision of individual NPs with surfaces. Such collisions are encountered in different analytical and electroanalytical situations. Irreversible adsorption of a target NP is generally sought in the design of nanobead-based microfluidic biosensors. The first explored example employs 300 nm magnetic maghemite nanobeads flowing through a microfluidic channel. NP collision and interaction with metallic surface are usually studied in the electrochemical nanoimpact strategy. The second example is illustrated here with either dielectric 100 nm PS NPs or 40 and 60 nm metallic Ag NPs.

3.2.1 Sensing Single Nanobead Attachment on an Au Sensor in a Microfluidic Environment

Commercial 300 nm carboxy-functionalized maghemite NPs were dissolved into a milli-Q water solution at a concentration of 10^8 NPs/mL. This solution was injected into a microfluidic channel constructed from an Ibidi sticky-slide® of 5×0.8 mm^2 section mounted atop an Au-coated Si substrate. The Au surface is used as the NP sensing or the recognition platform. The dimension of the sensor in contact with the solution of NPs is 5×10 mm^2 and only a 1×1 mm^2 surface at the stream front is imaged, as shown in Fig. 3a. To permit the capture of the NPs, the Au surface, corresponding to

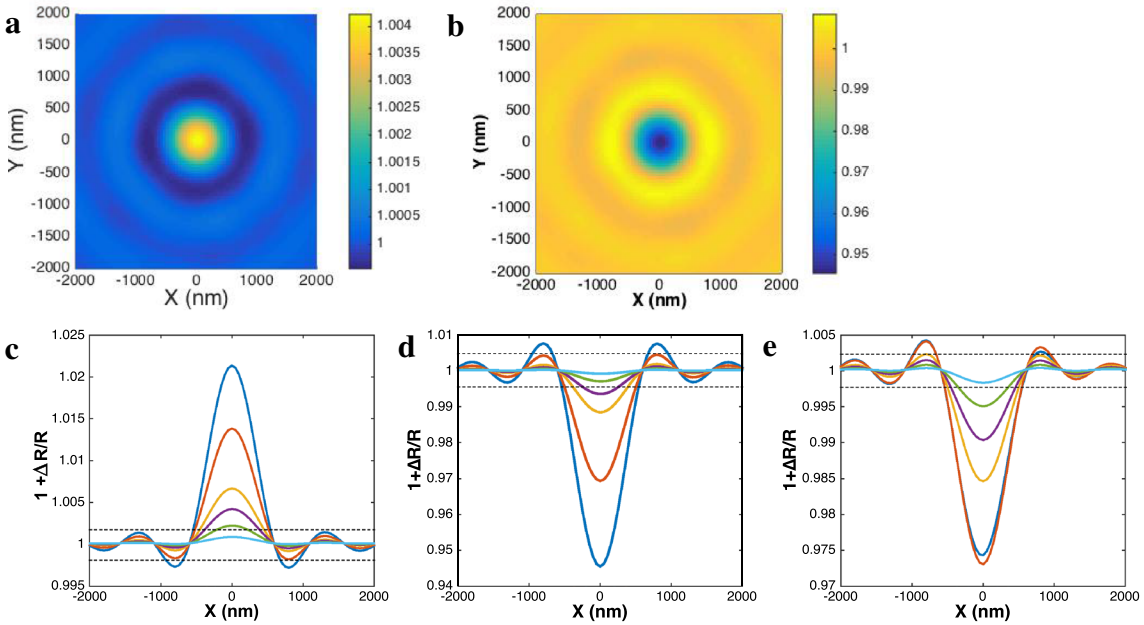

Fig. 2 Simulated reflectance images of a **a** 40 nm Ag and **b** 100 nm PS NPs located at the center of the image. Reflected intensity line profile along the y or x axis as a function of the NP size for **c** Ag, **d** PS and **e** Fe_3O_4 NPs of diameter 20, 30, 40, 50, 75 and 100 nm; dashed lines correspond to the ± 0.002 limit of detection for the reflectance measurement

the bottom surface of the channel, is functionalized by dip-coating with a thin layer of polyethyleneimine (ca. < 10 nm). This modified surface is denoted Au/PEI. At the natural pH of the milli-Q water, the Au/PEI presents a positive charge facing the flowing aqueous colloidal solution. This enables electrostatic interaction with the negatively charged NPs, and, therefore, the capture of the NPs. The sensor surface reflectivity is then monitored while circulating the colloidal solution at a low magnification, with a 10 × objective microscope. Images of the light reflected by the Au/PEI surface are taken from the top through the Ibidi slide cover and the colloidal solution. This allows probing the largest possible regions of the sensor, typically 1 mm^2, which for example can evidence capture dynamics heterogeneities, but is at the detriment of the image resolution (1px is ca. 1 μm^2).

Figure 3a–c shows selected snapshots of the Au/PEI surface taken (a) while a pure water solution was flowing (absence of NP) in the channel with a fluid velocity of 4 mm/s (flow rate 1 mL/min), then (b, c), respectively, 5.4 and 72 s after the detection of the first adsorption events resulting from the flow of the colloidal NP solution.

Different features can be identified on these images (zoom in Fig. 3a'–c'). Dark spots appearing on the surface correspond to individual adsorbed NPs (examples

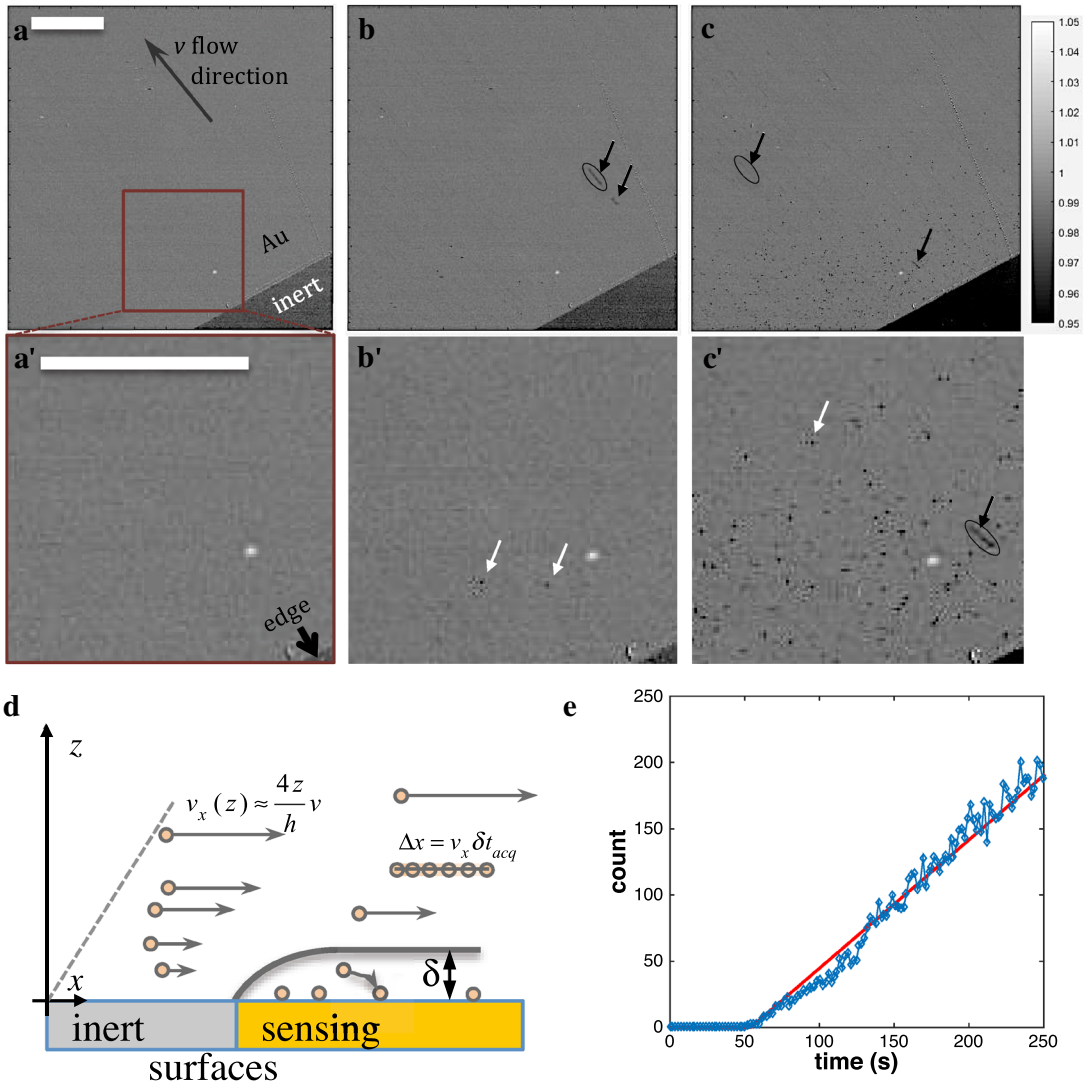

Fig. 3 Images of the bottom surface of a microfluidic channel during the flow of solution **a** before and **b**, **c** after injection of 300 nm maghemite colloidal solution. **b** and **c** are taken, respectively, 5.4 and 72 s after the first NP adsorption event is detected (5.4 s after **a**). **a'–c'** Zoomed selections from **a**–**c**. Bar = 200 μm. Arrows on the images show some examples of flowing (black arrows) or adsorbed (non-moving, white arrows) NPs. **d** Scheme describing the convective layer of thickness δ from which NPs are captured and how to estimate NP altitude from the length Δx of linear segments (image acquisition $\delta_{tacq} = 300$ ms) and the local velocity expression (assuming $z \ll h$ and with v the fow velocity expressed at mid-channel height $z = h/2$). **e** Evolution of the number of adsorbed NP counted (blue symbols) over the images in **a**–**c** and compared to Eq. 6 (red line)

pointed by white arrows in Fig. 3b', c'). They can be differentiated from NPs moving downstream, identified as the linear segment trajectories caught during the 300-ms camera exposure. Although they are not in the focal plane of the observation, the camera can catch these moving NPs to the point of estimating their individual velocity, v_x. The examples circled in Fig. 3b, c yield NPs with velocities $v_x = 250$ and 950 µm/s. From such particle trajectory tracking, one is then able, as schematized in Fig. 3d, to estimate the altitude of the NP or, as discussed elsewhere, to probe, with a resolution dictated by the NP dimension, the fluid flow dynamics [41]. Here, assuming the NPs are submitted to a parabolic Poiseuille flow profile, one can infer the moving NPs altitude from the Au substrate and along the $h = 800$ µm channel height. The example velocities suggest that the NPs are localized between 12.5 and 48 µm from the sensor surface. Interestingly the visualization from the top and through the solution allows visualizing and detecting NPs present in solution, even though they are out of focus.

These images also suggest, as proposed by the optical model, that FeOx NPs can readily be detected by reflectivity measurements. However, the low magnification cannot strictly be compared to the model as each NP is detected as an individual (1 pixel) spot of negative contrast (lesser reflectivity than the original Au/PEI substrate). In average, the different spots correspond to a ca. $2.2 \pm 0.4\%$ loss of reflectivity ($1 + \Delta R/R < 0.978 \pm 0.004$), which compares the reflectivity change predicted for 100 nm FeOx NPs in Fig. 2e ($1 + \Delta R/R = 0.975$).

Such optical monitoring also provides further information in NP-based sensing applications [42–44]. The number of NPs captured by the sensor, for example within the selected zoomed region, can be counted over time through the dark spot detection on each image. It allows inspecting the NP capture dynamics. For efficient adsorption events (with probability close to 1), the capture is mass transfer limited and the NP capture frequency is expected to reflect the NP mass transfer properties. Here, large flow rates over large sensor length along the flow direction, $l = 1$ cm, compared to the channel height, $h = 0.8$ mm, are used. Under these conditions, the only target NPs that can be captured by the sensor are coming from a thin depletion layer adjacent to the sensor, as schematized in Fig. 3d. The thickness of this depletion layer, δ, within the microfluidic convective regime scales as the inverse of the third root of the flow rate, v; the higher the flow rate is, the thinner the δ:

$$\delta \sim \frac{1}{v^{1/3}}. \tag{5}$$

The frequency of NP capture per cm^2 of sensor surface area, f_{surf}, then relies on the flux of NPs reaching the sensor surface by diffusion within this diffusion layer δ. Newman [45] computed this situation, which may also be computed from Comsol® [46]. For large velocities, one obtains:

$$f_{surf} = 0.81 D_{NP} C_{NP} \left(\frac{v}{D_{NP} l h} \right)^{1/3}, \tag{6}$$

with D_{NP} and C_{NP}, the NP diffusion coefficient and concentration in the colloidal solution, respectively. For the 10^8 NP/mL colloidal solution of 300 nm NPs of $D_{NP} = 1.6$ µm^2/s, the NP captured is then expected to increase linearly with time, with a slope equal to f_{surf}. Figure 3e shows that the experimental number of NPs capture indeed follows such linear trend with a slope of 9.5×10^2 NP/cm^2/s, in good agreement with the value of the mass transfer-limited flux density of 9×10^2 NP/cm^2/s obtained from (6). This particularly suggests that such imaging configuration allows not only probing the NPs concentration in the solution from their capture frequency, but also differentiating NPs freely moving in solution (out of focus) from adsorbed ones.

3.2.2 Visualizing Single Sub-100 nm Nanoparticle Immobilization on a Sensing Au Surface

Adsorption of NPs is also an important issue in the electrochemistry of individual NPs. Different authors [47–50] demonstrated that when large dielectric insulating spheres (from 150 nm to µm) collide with an UME, they irreversibly adsorb onto it. This adsorption sufficiently blocks the mass transfer of a redox probe toward the UME so that each individual adsorption event can be monitored electrochemically from a step-like transient (decrease) in UME current. Fodsick et al. later confirmed this hypothesis from the simultaneous optical and electrochemical visualization of the irreversible adsorption of fluorescent-labelled microspheres [50].

The dynamics of PS NPs collision with an Au surface was imaged through a water-immersion objective (40×, NA 0.8) immersed directly in a colloidal solution of PS NPs, as schematized in Fig. 1c. Figure 4a presents 100×75 µm^2 ROIs of reflectivity images of the Au surface (separated by 350-s interval) after it was contacted with 5 mL of milli-Q water colloidal solution of 100 nm PS NPs. Clearly these images show diffraction-limited dark, less reflecting, features appearing on the Au surface over time (see arrows in zoomed 25×25 µm^2 ROIs in Fig. 4a').

The evolution of the reflected light variation along lines crossing two examples of NPs were extracted from images and compared in Fig. 4b to the predicted profiles. If the profile widths are consistent with diffraction-limited imaged nanoobjects, the reflectivity variations, ΔR/R, corresponding to the different NPs detected are within -0.7 and -1.4%, which based on the proposed model suggests the detection of NPs with equivalent size between 40 and

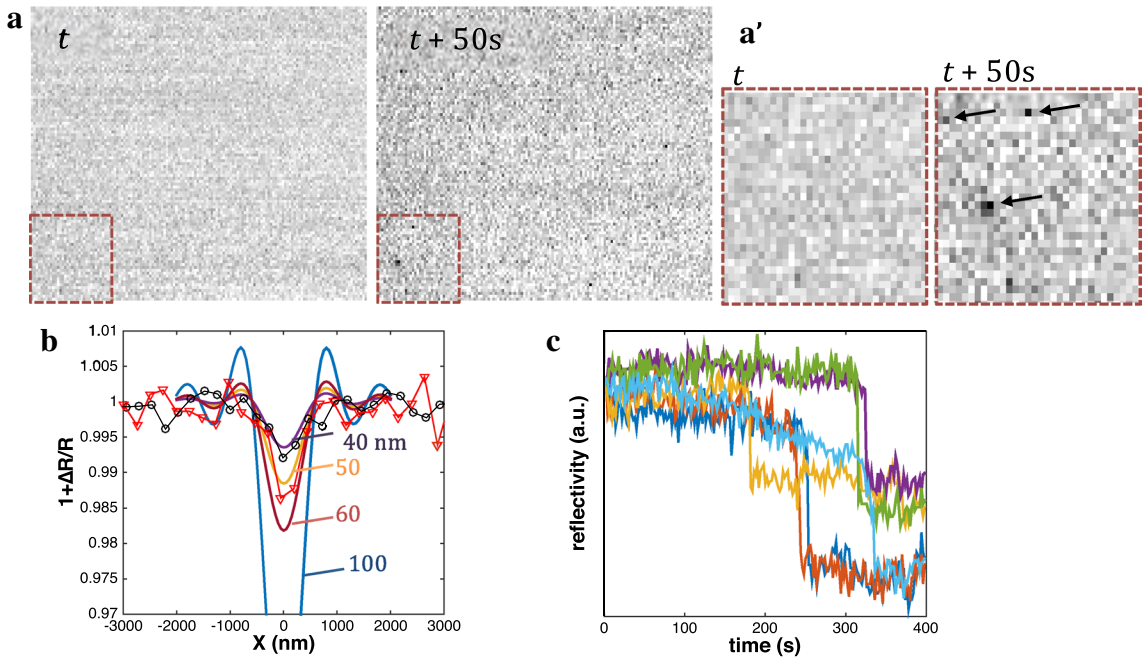

Fig. 4 Au surface reflectivity imaging of the adsorption of 100 nm PS NPs from a milli-Q water solution. **a** Examples of a 100×75 μm^2 ROI of reflectivity images taken 350 s apart, with zoom of the red ROI in **a'**. **b** Reflectivity change profile along selected lines; experimental data (points) compared to model profiles (lines) for, respectively, 40, 50, 60 and 100 nm. **c** Examples of the dynamics of selected single NPs adsorption events through the recording of local reflectivity variation at selected pixel positions over time

50 nm. This discrepancy is owing to the relative nature of the measurement and rather suggests that the Au substrate is more reflective than predicted: it would result in a higher background reflectance and of a lower relative reflectance change for the NPs.

The adsorption dynamic of individual NPs was also monitored. As shown in Fig. 4c for the variations of local reflectivity at selected point positions on the images, the adsorption of single NPs is instantaneous at the experimental acquisition rate ($\lesssim$300 ms). Finally, the superlocalization of the centroid of the PS NPs along time suggests that the NPs are strongly bound to the Au surface and do not noticeably move during tens of seconds. The same conclusions are drawn for other NPs that keep adsorbing as time goes. In agreement with earlier reports for larger dielectric polymeric spheres, the collision of the PS NPs leads to irreversible adsorption events.

Metallic or electrochemically active NPs can also be detected from a current (or potential) transient recorded while they collide onto a polarized electrode. A variety of nanomaterials have been probed from such electrochemical nanoimpact strategy. From the variety of current-transient features or from the frequency of collision events, different NP-electrode collision scenarii were proposed: from irreversible adsorption to repetitive bouncing (or electrode-surface detachment) of NPs. The latter multiple-bites collision of a same NP on an electrode is easily inferred for the collision of catalytic Pt NPs [32]. The same conclusion was also inferred in the case of the irreversible transformation of NPs upon their collision to the UME, such as the oxidative electrodissolution of Ag NPs. The sub-ms resolution of single-NP current transients shows multiple time-separated current spikes related to the multistep incomplete electrochemical dissolution of Ag NPs [51]. This was confirmed from Monte Carlo or multiphysic modeling of the NP Brownian motion during the electrochemical nanoimpact process suggesting indeed the possible escape of NPs after a short and incomplete charge transfer [52–54]. In principle, these situations may be differentiated optically. The optical monitoring, in 3D [11–14] by holography or in 2D by SPR [7, 8, 55, 56], of the reaction did not show such significant NP escape but rather that the NP stays close by ($<$300 nm) to the electrode surface until its complete dissolution. On one hand, these experiments then suggest that if NPs are partially dissolved, allowing their desorption, they may not be evacuated in the solution, at least with the Brownian dynamics of a freely diffusing NP. On the other hand, the probability of NP escape from the electrode can be increased when the electrochemical cell dimension is reduced [57]. Indeed, by confining the NP into the end of a nanopipette, the probability of NP ejection from the electrode, imaged by fluorescence microscopy, increases as a result of the increasing importance of the electrostatic repulsion of the NP by the nanopipette walls. Although this points to the importance of

electrostatic effects when decreasing the electrochemical cell volume, it may differ from the situation encountered in most electrochemical nanoimpacts studies.

To advocate for such phenomena, we have monitored the collision of individual Ag NPs with a Au surface in the absence of applied electrochemical potential, therefore, avoiding the complicated NPs dissolution leading to their optical disappearance. The dynamics of Ag NPs collision at a non-polarized Au surface was imaged through a water-immersion objective (40×, NA 0.8) immersed directly in the colloidal solution, as schematized in Fig. 1c.

The reflectivity of an Au surface in contact with a solution, made of 10µL of a 0.02 mg/mL 60 nm Ag NPs diluted in 5 mL milli-Q water (final Ag NP concentration $C_{NP} = 3.5 \times 10^7$ NP/mL) was imaged. Figure 5a presents successive frames of a selected 50×50 µm^2 ROI of the Au surface. As for FeOx and PS NPs, diffraction-limited dark features considered as NPs are observed on these frames. At the observation frequency, these features are now moving over successive frames and no irreversible adsorption of the NPs could be monitored. This is confirmed from Fig. 5b, which presents the average local reflectivity variation measured over even smaller ROI (1×1 µm^2 or 10×10 µm^2). Indeed, single or multiple individual reflectivity spikes are detected over the entire movie. These reflectivity spikes differ from the steps recorded for PS NPs and show that single or, at best, 2 NPs appear and disappear stochastically from these small ROIs. Similarly, Fig. 5c presents the counting of dark features appearing over time over a larger 125×100 µm^2 ROI of the Au substrate. Individual NPs also occasionally appear in this ROI, but the amount of NPs does not increase as is expected for irreversible adsorption processes (for FeOx NPs, see Fig. 3e). These observations suggest that Ag NPs do not adsorb irreversibly on the Au surface and are rather exploring, by Brownian motion, large areas of the Au surface.

The maximum steady-state mass transfer-limited flux density of NPs per surface area reaching the ROI of surface area $S = 1.3 \times 10^{-4}$ cm^2 can be approximated (For a disk of radius a UME the flux of diffusing NP is given by $4D_{NP}C_{NP}a$ with $S = \pi a^2$ yielding to a flux density $f = 4 D_{NP}C_{NP}/\pi^{1/2}S^{1/2} = 2.25\ D_{NP}C_{NP}/S^{1/2}$. For a square UME of side length l [12], the flux is given by $\pi/2^{1/2}\ D_{NP}C_{NP}l$ and $S = l^2$ yielding to a flux density $f = 2.22\ D_{NP}C_{NP}/S^{1/2}$) by $f_{surf} \approx 2.2 D_{NP}C_{NP}/S^{1/2}$ with $D_{NP} = 8.3$ µm^2/s for 60 nm NPs. A density frequency of 5.6×10^2 NP/cm^2/s, or equivalently a frequency of 0.07 NP/s would then be expected over the 100×125 µm^2 ROI. This suggests that over the ca. 100 s, one would be able to detect ca. 7 NPs, which is in agreement with the average number of NPs, ca. 2, constantly detected in Fig. 5c. Meanwhile, the successive frames in Fig. 5a suggest that the same NPs are counted several times even though not on the same position of the ROI. This agrees with the features of constrained Brownian motion generally observed when Brownian nanoobjects trajectories are analyzed close to walls. It also agrees with the multi-bites nanoimpacts or bouncing NPs postulated earlier [51–54]. These multiple bouncing collisions can be detected optically here with Ag

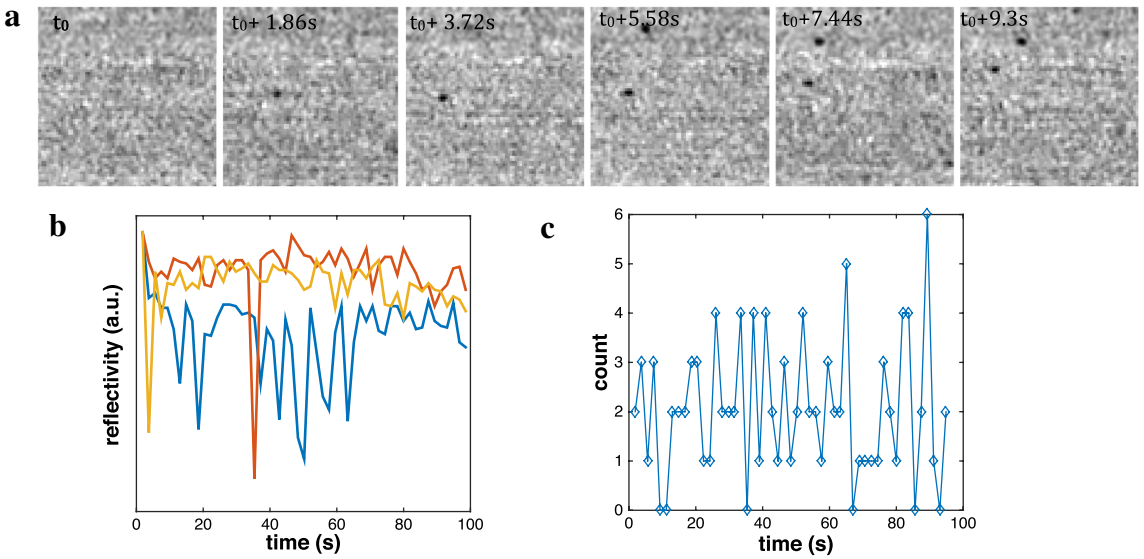

Fig. 5 Reflectivity monitoring of 60 nm bouncing Ag NPs in milli-Q water (<20 µM citrate) solution. **a** A same 50×50 µm^2 region of interest (ROI) is presented over successive frames (acquisition time 50 ms) taken every 1.8 s: two dark features, considered as NPs, are changing location between frames; **b** stochastic reflectivity spikes detected from local reflectivity averaged over 1×1 µm^2 (yellow and orange traces) or 10×10 µm^2 (blue trace) ROIs; **c** number of NPs counted over a 125×100 µm^2 ROI: the number of NPs detected above the Au surface is constant over time

NPs since the NPs are not subjected to any electrochemical transformation (dissolution).

The bouncing of Ag NPs may seem at odds with earlier correlated optical observation of their dissolutive electrochemical nanoimpacts [7, 11, 55]. It is likely due to the repulsive interaction between the stabilized citrate-capped NPs and the Au surface. Indeed, their behavior is drastically altered when electrolyte is present in the solution. This can be performed, either by adding a 1 mL 20 mM NaCl solution to the 5 mL Ag NP milli-Q solution or by injecting aliquots of stock Ag NP solutions to a 10 mM NaCl solution. Figure 6 illustrates such experiment in which a first 5µL aliquot of 40 nm Ag NPs (final C_{NP}=6 10^7 NP/mL) is injected into a 5 mL NaCl 10 mM solution at t=48 s, followed by the injection of a second 10µL aliquot of 60 nm Ag NPs (final C_{NP}=3.5 10^7 NP/mL) at t=200 s. Figure 6a shows the images taken after injection and at the end of the experiment of a 100×75 µm^2 ROI showing the coverage of the Au surface by multiple dark features. A series of zoomed images of a 10×10 µm^2 ROI of the Au surface recorded during this experiment are also displayed for t=74.4, 100.4, 148.8, 186 s, showing that these dark features are now fixed over the same location, suggesting their irreversible adsorption. Some optical intensity profile lines of selected dark features also suggests that they correspond to diffraction-limited objects, supposedly NPs. From these profiles, it also seems that the optical reflectivity decreases for larger NP sizes. These observations, as those made in the absence of NaCl, suggest that Ag NPs can be detected by simple microscopic observation in a reflection mode, even though the loss of reflectivity is at odds with the optical prediction (gain in reflectivity) presented above.

Selected examples of the time evolution of the local reflectivity variation estimated over different 1 µm^2 ROIs are presented in Fig. 6b. This contrasts totally from the stochastic NP bouncing detected in the absence of NaCl. Indeed, reflectivity steps are now detected, suggesting the irreversible adsorption of the NPs in the presence of NaCl.

The same conclusion is drawn from the evolution of the number of dark features counted over the 100×75 µm^2 ROI of the Au surface (Fig. 6c). Apart from a short time interval following each injection, where optical perturbations may lead to an artificial increase in NP surface population, the number of NPs steadily increases over the time. The flux of NPs reaching the Au surface is fed by NP linear diffusion from the solution while the Au surface continuously removes

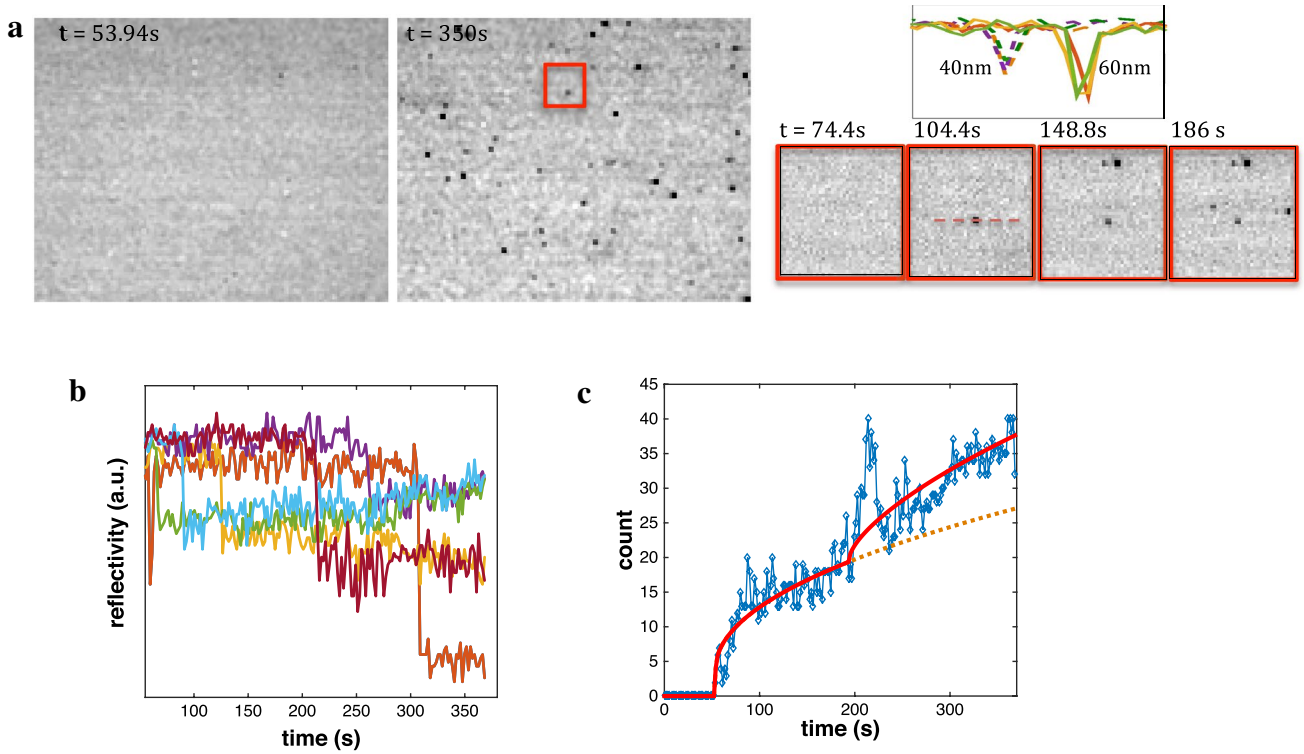

Fig. 6 Reflectivity imaging of 40 and 60 nm Ag NPs irreversible adsorption onto a reflecting Au surface upon injection of aliquots of 40 (at t=53 s) and 60 nm (at t=200 s) of NP solutions into a 5 mL 10 mM NaCl solution. **a** Examples of reflectivity images of a 100×75 µm^2 ROI of the Au surface with zoomed 10×10 µm^2 ROI at t=74.4, 100.4, 148.8, 186 s and examples of reflectivity profile lines of selected 40 (left) and 60 (right) nm Ag NPs. **b** Examples of reflectivity transients showing the irreversible NPs adsorption. **c** Evolution of the number of NPs counted over the 100×75 µm^2 ROI in **a** compared with planar diffusion Eq. (8)

them from the solution. This is conceptually analogous to the dissolutive electrochemical nanoimpact experiments, except that the NPs here are not dissolved, only irreversibly adsorbed, at the Au surface. One can then estimate this flux from the knowledge of the NP content in solution, C_{NP}. It is anticipated that the NP mass transfer or frequency, f, is given by linear diffusion profile [43], following Cottrell's law, then:

$$f = \frac{SC_{NP}D_{NP}}{\sqrt{\pi D_{NP}t}}, \tag{7}$$

from which the number of NPs reaching the Au surface, $n_{NP}(t)$, is obtained by integration:

$$n_{NP}(t) = 2C_{NP}S\sqrt{\frac{D_{NP}t}{\pi}}. \tag{8}$$

The two solid lines in Fig. 6c present the predicted variations from Eq. (8) for, respectively, the 40 nm (faster diffusing and more concentrated) and 60 nm NPs. The sum of these curves reproduces nicely the experimental variations. The fit of the experimental variations is obtained with $C_{NP40}=4.5\times10^7$ NP/mL and $C_{NP60}=3.4\times10^7$ NP/mL, which compares well with the respective expected values of 6 and 3.5×10^7 NP/mL.

It then suggests that the increasing number of dark features adsorbing on the Au surface are nanoobjects present at the same concentration and moving analogously with the injected Ag NPs. We attribute these dark features to individual Ag NPs. It cannot be excluded that for the 40 nm NPs dimers or agglomerates are preferentially detected.

This demonstration of irreversible and quantitative (mass transfer limited) adsorption of Ag NPs on surfaces when they are in electrolytic solution (at least > 10 mM here) suggests that care should be taken when performing or interpreting electrochemical nanoimpacts. It is frequently assumed that NPs remain stable in electrolytic solutions. But dissolved salts can have many effects on the NPs and their local environment as modifying the pH, increasing the ionic strength, desorbing the NP capping agent, etc. The consequences on the NP behavior also depend on the NP size, the NP shape, the capping agents, or the chosen electrolyte. The NP stability is, therefore, difficult to predict and has to be investigated for new experimental conditions prior to nanoimpacts experiments upon the possibility of making mistakes in evaluating the NP size dispersion based on spike charges and/or the NP concentration based on the impact frequency. This is one of the reasons why nanoimpacts are more and more coupled to a second complementary analysis technique. The effect of electrolytic solution on NP aggregation was for example demonstrated from solution phase NP tracking [58, 59]. Here, we use the reflectance microscopy to highlight the importance of surface adsorption effects. The introduction of NaCl, even at the 10 mM level seems to strongly affect the NP environment and its interaction with a surface, even in the absence of electrochemical polarization. By destabilizing the colloidal solution, the NPs tend to adsorb irreversibly on surfaces. This study shows that reflectance microscopy is an elegant way for further study in situ the effect of the chemical and physical (such as size, charge, or polarizability) nature of the ions of an electrolyte to destabilize colloidal NPs. For polymeric or biologic nanomaterials or nanoparticles coated by such constituents, the nature of each ionic component of an electrolyte is indeed known to alter (chaotropic effect) or promote (kosmotropic effect) hydrogen bonds networks yielding in, respectively, the destabilization or stabilization of their colloidal solutions. Similar studies could be envisioned under optical monitoring or electrochemical actuation.

From the electrochemical nanoimpact prospect, it suggests that even if multiple bytes current transients have been previously detected electrochemically [51–53], the adsorption strength is stronger than the suggested escape of the NP into the solution, at least over distances larger than > 300 nm.

Another possible reason should then be invoked to explain the multiple dissolutive bites observed electrochemically. The presence of oxide or pseudo-halide shell layer, or even its formation during the oxidative process, in the presence of residual halide ions, even at the sub-mM level, could impair the NP-electrode contact resistance and the overall electrodissolution process. The role of such oxide layer on Ag NP dissolution was recently demonstrated from single-NP optical birefringence visualization [60, 61].

Moreover, the irreversible adsorption of NPs will apparently decrease the NP solution content especially in high surface-to-volume cell configurations: such as small volume pipetting or high dilution processes, or maybe in nanoelectrochemical cell. Similarly, the adsorption of NPs to the UME insulating walls [62] may also be a strong competing source of NP depletion, which can be taken into account by readjusting the frequency-C_{NP} relationship. It may for example explain the often observed decrease of NP impact frequency over long acquisition times (as predicted by the establishment of a pseudo-linear diffusion regime expected over cylindrical UMEs [34]).

Finally, Ag NPs are experimentally detected as dark features, which is at odds with the optical prediction. If some bright feature may be detected, the majority of features (> 95%) are darker. Such discrepancies can account for the selection of incorrect values of the Au substrate and/or solution and/or Ag NP refractive indexes in the model. Slight alterations of the Au and solution indexes could indeed change the amount of reflected light. However, pure Ag NPs should still appear as bright features. One possibility could rather be that Ag NPs are covered by a thin layer of

oxide [60] (or AgCl) formed by their spontaneous oxidation in an O_2-saturated NaCl solution. It is difficult to evaluate precisely the effect of such a layer; however, from mean field approximation theories (such as Maxwell–Garnett) a 2 nm coating of AgCl over a 40 nm core Ag NP may yield a strong enough change in the apparent refractive index of the NP and explain the dark feature on an Au surface.

4 Conclusion

Dielectric and metallic NPs can be visualized at the single-NP level by simple imaging of the light reflected by a reflecting surface. An optical BEM modeling, extending Ünlü's work, predict that both dielectric PS and metallic NPs can be individually visualized, without any label, by collecting the local reflectance change of an Au surface. The model shows that such reflectivity imaging provides an interferometric detection, allowing one to enhance the optical detection sensitivity. If 30 nm NPs should be theoretically detected, it is anticipated that other reflecting substrates could be used similarly without needing dark-field illumination conditions. The further advantage of this interferometric detection is that dielectric NPs can also be detected, as negative contrast (dark or less reflecting) features, which is a considerable advantage compared to microscopies relying on dark-field illumination.

A microscope operating in the reflection mode was used to image, through solution, or even microfluidic cover, the dynamics of NP capture on an Au-sensing surface. First, starting with large 300 nm FeOx magnetic nanobeads in a microfluidic environment, it is shown how such NPs are optically detected, at the single-NP level, and counted. The strategy can be used to analyze the convective adsorption of NPs onto a large sensing area. This may be of interest for monitoring in real time and in situ the dynamics of nanoentities capture in microfluidic biosensors.

It can also be used to monitor electrochemical processes occurring at single NPs. Even if no electrochemical activation was used in this work, the Au surface monitored optically could also be polarized in an electrochemical configuration. The present work shows that individual 100 nm PS NPs as well as 40 and 60 nm Ag NPs can be imaged through a water-immersion objective directly immersed between a colloidal solution and the Au surface, from their ability to alter the local reflectivity of an Au surface. If PS NPs appear as dark features, in agreement with the predicted model, Ag NPs are detected similarly, although they should be detected as bright features. This is attributed to the likely presence of Ag oxide or halide layer. The dynamic monitoring of the NPs behavior over the Au surface shows that PS NPs strongly and irreversibly adsorb to Au. The same observation is made for Ag NPs when prepared in an electrolytic solution (10 mM NaCl), while in the absence of electrolyte, the multiple bouncing of the NPs is evidenced. This confirms previous simultaneous opto-electrochemical studies, which were at odds with multiple bouncing suggested from high time resolution electrochemical nanoimpacts. Ag NPs, in the absence of polarization, stand for tens of seconds on the Au surface, without showing Brownian exploration of the solution after they have contacted the electrode. We propose that the presence or formation of poorly conducting Ag oxide or halide may also explain the multiple electrochemical bites behavior.

As a perspective of this work, reflectance microscopy is a simple yet powerful tool that has allowed monitoring electrochemical processes [15–18, 63]. It does not require a transparent electrode unlike methods relying on dark-field illuminations, it is not restricted to Au electrodes, but to many reflecting surfaces [18], and can be performed at standard glass-insulated microelectrodes [16], or be coupled to local probing such as STM [63]. Based on these reported results, we expect that the technique could be applied to imaging the electrochemical reactivity of a wide range of NPs at the single entity level.

Acknowledgements We are grateful for financial support by the Agence Nationale pour la Recherche (NEOCASTIP ANR-15-CE09-0015-02 project) and Direction Générale de l'Armement (AMMIB ANR-13-ASTR-0021-01), by Universities Paris Diderot and Paris Sud and by CNRS.

References

1. Bard AJ, Mirkin MV, editors. Scanning electrochemical microscopy. 2nd ed. Boca Raton: CRC Press; 2012.
2. Bentley CL, Kang M, Unwin PR. Scanning electrochemical cell microscopy: new perspectives on electrode processes in action. Curr Opin Electrochem. 2017;6:23–30.
3. Shan XN, Patel U, Wang SP, Iglesias R, Tao NJ. Imaging local electrochemical current via surface plasmon resonance. Science. 2010;327:1363–6.
4. Shan XN, Diez-Perez I, Wang LJ, Wiktor P, Gu Y, Zhang LH, Wang W, Lu J, Wang SP, Gong QH, Li JH, Tao NJ. Imaging the electrocatalytic activity of single nanoparticles. Nat Nanotech. 2012;7:668–72.
5. Fang YM, Wang W, Wo X, Luo YS, Yin SW, Wang YX, Shan XN, Tao NJ. Plasmonic imaging of electrochemical oxidation of single nanoparticles. J Am Chem Soc. 2014;136:12584–7.
6. Yuan T, Wang W. Studying the electrochemistry of single nanoparticles with surface plasmon resonance microscopy. Curr Opin Electrochem. 2017;1:17–22.
7. Nizamov S, Kasian O, Mirsky VM. Individual detection and electrochemically assisted identification of adsorbed nanoparticles by using surface plasmon microscopy. Angew Chem Int Ed. 2016;55:7247–51.
8. Nizamov S, Scherbahn V, Mirsky VM. Detection and quantification of single engineered nanoparticles in complex samples using template matching in wide-field surface plasmon microscopy. Anal Chem. 2016;88:10206–14.

9. Peng Y, Xiong B, Peng L, Li H, He Y, Yeung ES. Recent advances in optical imaging with anisotropic plasmonic nanoparticles. Anal Chem. 2015;87:200–15.
10. Jing C, Reichert J. Nanoscale electrochemistry in the "dark-field". Curr Opin Electrochem. 2017;6:10–6.
11. Brasiliense V, Berto P, Combellas C, Tessier G, Kanoufi F. Electrochemistry of single nanodomains revealed by three-dimensional holographic microscopy. Acc Chem Res. 2016;49:2049–57.
12. Brasiliense V, Patel AN, Martinez-Marrades A, Shi J, Chen Y, Combellas C, Tessier G, Kanoufi F. Correlated electrochemical and optical detection reveals the chemical reactivity of individual silver nanoparticles. J. Am Chem Soc. 2016;138:3478–83.
13. Patel AN, Martinez-Marrades A, Brasiliense V, Koshelev D, Besbes M, Kuszelewicz R, Combellas C, Tessier G, Kanoufi F. Deciphering the elementary steps of transport-reaction processes at individual Ag nanoparticles by 3D superlocalization microscopy. Nano Lett. 2015;15:6454–63.
14. Batchelor-McAuley C, Martinez-Marrades A, Tschulik K, Patel AN, Combellas C, Kanoufi F, Tessier G, Compton RG. Simultaneous electrochemical and 3D optical imaging of silver nanoparticle oxidation. Chem Phys Lett. 2014;597:20–5.
15. Munteanu S, Garraud N, Roger JP, Amiot F, Shi J, Chen Y, Combellas C, Kanoufi F. In situ, real time monitoring of surface transformation: ellipsometric microscopy imaging of electrografting at microstructured gold surfaces. Anal Chem. 2013;85:1965–71.
16. Munteanu S, Roger JP, Fedala Y, Amiot F, Combellas C, Tessier G, Kanoufi F. Mapping fluxes of radicals from the combination of electrochemical activation and optical microscopy. Faraday Discuss. 2013;164:241–58.
17. Fedala Y, Munteanu S, Kanoufi F, Tessier G, Roger JP, Wu C, Amiot F. Calibration procedures for quantitative multiple wavelengths reflectance microscopy. Rev Sci Instrum. 2016;87:013702.
18. Chakri S, Patel AN, Frateur I, Kanoufi F, Sutter EM, Mai Tran TT, Tribollet B, Vivier V. Imaging of a thin oxide film formation from the combination of surface reflectivity and electrochemical methods. Anal Chem. 2017;89:5303–10.
19. van Dijk MA, Lippitz M, Orrit M. Far-field optical microscopy of single metal nanoparticles. Acc Chem Res. 2005;38:594–601.
20. van Dijk MA, Lippitz M, Stolwijk D, Orrit M. A common-path interferometer for time-resolved and shot-noise-limited detection of single nanoparticles. Opt Express. 2007;15:2273–87.
21. Lindfors K, Kalkbrenner T, Stoller P, Sandoghdar V. Detection and spectroscopy of gold nanoparticles using supercontinuum white light confocal microscopy. Phys Rev Lett. 2004;93:037401.
22. Kukura P, Ewers H, Müller C, Renn A, Helenius A, Sandoghdar V. High-speed nanoscopic tracking of the position and orientation of a single virus. Nat. Methods. 2009;6:923–7.
23. Ortega-Arroyo J, Kukura P. Interferometric scattering microscopy (iSCAT): new frontiers in ultrafast and ultrasensitive optical microscopy. Phys Chem Chem Phys. 2012;14:15625–36.
24. Sevenler D, Avci O, Ünlü MS. Quantitative interferometric reflectance imaging for the detection and measurement of biological nanoparticles. Biomed Opt Express. 2017;8:2976–89.
25. Avci O, Adato R, Ozkumur AY, Ünlü MS. Physical modeling of interference enhanced imaging and characterization of single nanoparticles. Opt Express. 2016;24:6094–114.
26. Avci O, Ünlü NL, Ozkumur AY, Ünlü MS. Interferometric reflectance imaging sensor (iris) - a platform technology for multiplexed diagnostics and digital detection. Sensors. 2015;15:17649–65.
27. Boccara M, Fedala Y, Bryan CV, Bailly-Bechet M, Bowler C, Boccara C. Full-field interferometry for counting and differentiating aquatic biotic nanoparticles: from laboratory to Tara Oceans. Biomed. Opt Express. 2016;7:3736–46.
28. Lemineur J-F, Noël J-M, Ausserré D, Combellas C, Kanoufi F. Combining electrodeposition and optical microscopy for probing size-dependent single-nanoparticle electrochemistry. Angew Chem Int Ed. 2018;57:11998–2002.
29. Lemineur J-F, Noël J-M, Combellas C, Ausserré D, Kanoufi F. The promise of antireflective gold electrodes for optically monitoring the electrodeposition of single silver nanoparticles. Faraday Discuss. 2018;210:381–95.
30. Stockmann TJ, Lemineur J-F, Liu H, Cometto C, Robert M, Combellas C, Kanoufi F. Single $LiBH_4$ nanocrystal stochastic impacts at a micro water vertical bar ionic liquid interface. Electrochim Acta. 2019;299:222–30.
31. Squires TM, Messinger RJ, Manalis SR. Making it stick: convection, reaction and diffusion in surface-based biosensors. Nat Biotech. 2008;26:417–26.
32. Xiao X, Bard AJ. Observing single nanoparticle collisions at an ultramicroelectrode by electrocatalytic amplification. J. Am Chem Soc. 2007;129:9610–2.
33. Zhou YG, Rees NV, Compton RG. The electrochemical detection and characterization of silver nanoparticles in aqueous solution. Angew Chem Int Ed. 2011;50:4219–21.
34. Sokolov SV, Eloul S, Kätelhön E, Batchelor-McAuley C, Compton RG. Electrode-particle impacts: a users guide. Phys Chem Chem Phys. 2017;19:28–43.
35. Garcia de Abajo FJ, Howie A. Retarded field calculation of electron energy loss in inhomogeneous dielectrics. Phys Rev B. 2002;65:115418.
36. Hohenester U, Trügler A. MNPBEM – A Matlab toolbox for the simulation of plasmonic nanoparticles. Comput Phys Commun. 2012;183:370–81.
37. Waxenegger J, Hohenester U, Trügler A. Plasmonics simulations with the MNPBEM toolbox: consideration of substrates and layer structures. Comput Phys Commun. 2015;193:138–50.
38. MNPBEM toolbox. 2018. http://physik.uni-graz.at/mnpbem/. Accessed 20 Dec 2018.
39. Codes developed for the SP-IRIS. 2018. https://github.com/derinsevenler/SP-IRIS-BEM. Accessed 20 Dec 2018.
40. Refractive index values are tabulated. 2018. https://refractiveindex.info/. Accessed 20 Dec 2018.
41. Brasiliense V, Berto P, Aubertin P, Maisonhaute E, Combellas C, Tessier G, Courty A, Kanoufi F. Light driven design of dynamical thermosensitive plasmonic superstructures: a bottom-up approach using silver supercrystals. ACS Nano. 2018;12:10833–42.
42. Wang W, Tao NJ. Detection, counting, and imaging of single nanoparticles. Anal Chem. 2014;86:2–14.
43. Wo X, Li Z, Jiang Y, Li M, Su Y-W, Wang W, Tao NJ. Determining the absolute concentration of nanoparticles without calibration factor by visualizing the dynamic processes of interfacial adsorption. Anal Chem. 2016;88:2380–5.
44. Kuzmichev A, Skolnik J, Zybin A, Hergenröder R. Absolute analysis of nanoparticle suspension with surface plasmon microscopy. Anal Chem. 2018;90:10732–7.
45. Newman J. The fundamental principles of current distribution and mass transport in electrochemical cells. In: Bard AJ, editor. Electroanalytical chemistry, vol. 6. New York: Dekker; 1973. p. 279–97.
46. Fuchs A, Fermigier M, Combellas C, Kanoufi F. Scanning electrochemical microscopy. Hydrodynamics generated by the motion of a scanning tip and its consequences on the tip current. Anal Chem. 2005;77:7966–75.
47. Quinn BM, van't Ho PG, Lemay SG. Time-resolved electrochemical detection of discrete adsorption events. J Am Chem Soc. 2004;126:8360–1.
48. Boika A, Thorgaard SN, Bard AJ. Monitoring the electrophoretic migration and adsorption of single insulating nanoparticles at ultramicroelectrodes. J Phys Chem B. 2013;117:4371–80.
49. Suraniti E, Kanoufi F, Gosse C, Zhao X, Dimova R, Pouligny B, Sojic N. Electrochemical detection of single microbeads

manipulated by optical tweezers in the vicinity of ultramicroelectrodes. Anal Chem. 2013;85:8902–9.
50. Fosdick SE, Anderson MJ, Nettleton EG, Crooks RM. Correlated electrochemical and optical tracking of discrete collision events. J Am Chem Soc. 2013;135:5994–7.
51. Oja SM, Robinson DA, Vitti NJ, Edwards MA, Liu Y, White HS, Zhang B. Observation of multipeak collision behavior during the electro-oxidation of single Ag nanoparticles. J Am Chem Soc. 2017;139:708–18.
52. Ma W, Ma H, Chen JF, Peng Y-Y, Yang Z-Y, Wang H-F, Ying Y-L, Tian H, Long Y-T. Tracking motion trajectories of individual nanoparticles using time-resolved current traces. Chem Sci. 2017;8:1854–61.
53. Ustarroz J, Kang M, Bullions E, Unwin PR. Impact and oxidation of single silver nanoparticles at electrode surfaces: one shot versus multiple events. Chem Sci. 2017;8:1841–53.
54. Robinson DA, Liu Y, Edwards MA, Vitti NJ, Oja SM, Zhang B, White HS. Collision dynamics during the electrooxidation of individual silver nanoparticles. J Am Chem Soc. 2017;139:16923–31.
55. Sun L, Fang Y, Li Z, Wang W, Chen H-Y. Simultaneous optical and electrochemical recording of single nanoparticle electrochemistry. Nano Res. 2017;10:1740–8.
56. Sun L, Wang W, Chen H-Y. Dynamic nanoparticle-substrate contacts regulate multi-peak behavior of single silver nanoparticle collisions. ChemElectroChem. 2018;5:2995–9.
57. Hao R, Fan Y, Zhang B. Imaging dynamic collision and oxidation of single silver nanoparticles at the electrode/solution interface. J Am Chem Soc. 2017;139:12274–82.
58. Robinson DA, Kondajji AM, Castañeda AD, Dasari R, Crooks RM, Stevenson KJ. Addressing colloidal stability for unambiguous electroanalysis of single nanoparticle impacts. J Phys Chem Lett. 2016;7:2512–7.
59. Sokolov SV, Tschulik K, Batchelor-McAuley C, Jurkschat K, Compton RG. Reversible or not? Distinguishing agglomeration and aggregation at the nanoscale. Anal Chem. 2015;87:10033–9.
60. Sundaresan V, Monaghan JW, Willets KA. Visualizing the effect of partial oxide formation on single silver nanoparticle electrodissolution. J Phys Chem C. 2018;122:3138–45.
61. Smith JG, Jain PK. The ligand shell as an energy barrier in surface reactions on transition metal nanoparticles. J Am Chem Soc. 2016;138:6765–73.
62. Eloul S, Compton RG. Shielding of a microdisc electrode surrounded by an adsorbing surface. ChemElectroChem. 2014;1:917–24.
63. Di N, Damian A, Maroun F, Allongue P. Influence of potential on the electrodeposition of co on Au(111) by in situ stm and reflectivity measurements. J Electrochem Soc. 2016;163:D3062–8.